Naval Research Laboratory
Washington, DC 20375-5320

NRL/5610/MR—2022/1

Structured Fog Obscuration Properties

MATTHEW HART

Aerosol Optics Section
Optical Science Division

PETER JUDD

Intelligence, Surveillance, and Reconnaissance Systems and Processing Section
Optical Science Division

ANKIT RAGHURAM

Optical Techniques Section
Optical Science Division

ABBIE WATNIK

Optical Physics Branch
Optical Science Division

September 20, 2022

REPORT DOCUMENTATION PAGE

Form Approved
OMB No. 0704-0188

1. REPORT DATE *(DD-MM-YYYY)*	**2. REPORT TYPE**	**3. DATES COVERED** *(From - To)*
20-09-2022	NRL Memorandum Report	05/01/2019 – 06/01/2021

4. TITLE AND SUBTITLE

Structured Fog Obscuration Properties

5a. CONTRACT NUMBER
N0001420WX00469

5b. GRANT NUMBER

5c. PROGRAM ELEMENT NUMBER
62271N

6. AUTHOR(S)

Matthew Hart, Peter Judd, Ankit Raghuram, and Abbie Watnik

5d. PROJECT NUMBER

5e. TASK NUMBER
0001

5f. WORK UNIT NUMBER
1E72

7. PERFORMING ORGANIZATION NAME(S) AND ADDRESS(ES)

Naval Research Laboratory
4555 Overlook Avenue, SW
Washington, DC 20375-5320

8. PERFORMING ORGANIZATION REPORT NUMBER

NRL/5610/MR--2022/1

9. SPONSORING / MONITORING AGENCY NAME(S) AND ADDRESS(ES)

Office of Naval Research
875 N Randolph Street
Arlington, VA 22217-1995

10. SPONSOR / MONITOR'S ACRONYM(S)

ONR

11. SPONSOR / MONITOR'S REPORT NUMBER(S)

12. DISTRIBUTION / AVAILABILITY STATEMENT

DISTRIBUTION STATEMENT A: Approved for public release; distribution is unlimited.

13. SUPPLEMENTARY NOTES

14. ABSTRACT

This work investigates the optical penetration of thermally produced infrared radiation through structured fog patterns and the assessment of the efficacy of various fog patterns that may lead to a technique to create artificial shrouds that are effective while also being minimally perceptible. Dynamic fog structures were created in front of geometrically shaped targets of various temperatures. The fog dynamics was controlled using timed spray nozzles in several different configurations with respect to the targets. Real time videos of the obscured scene were recorded in three bands: visible(VIS), mid-wavelength infra-red(MWIR) and long-wavelength infra-red(LWIR). Several approaches of machine learning are suggested to analyze the results and evaluate the ability to produce the desired effect from the structured fog.

15. SUBJECT TERMS

Fog
Obscuration
Machine learning
Artificial intelligence

16. SECURITY CLASSIFICATION OF:			**17. LIMITATION OF ABSTRACT**	**18. NUMBER OF PAGES**	**19a. NAME OF RESPONSIBLE PERSON**
					Matthew Hart
a. REPORT	**b. ABSTRACT**	**c. THIS PAGE**	U	20	**19b. TELEPHONE NUMBER** *(include area code)*
U	U	U			(202) 767-0122

This page intentionally left blank.

NRL Memorandum
Structured Fog Obscuration Properties (SFOP)
Work Unit:

Abstract

This work investigates the optical penetration of thermally produced infrared radiation through structured fog patterns and the assessment of the efficacy of various fog patterns that may lead to a technique to create artificial shrouds that are effective while also being minimally perceptible. Dynamic fog structures were created in front of geometrically shaped targets of various temperatures. The fog dynamics was controlled using timed spray nozzles in several different configurations with respect to the targets. Real time videos of the obscured scene were recorded in three bands: visible(VIS), mid-wavelength infra-red(MWIR) and long-wavelength infra-red(LWIR). Several approaches of machine learning are suggested to analyze the results and evaluate the ability to produce the desired effect from the structured fog.

Motivation

The presence of fog can be detrimental to the warfighter's ability to provide reliable situational awareness, likewise a strategically placed (localized) fog shroud can have the effect of acting as a barrier to protect against optically based reconnaissance. In the case of ship defense, the generation of an artificial fog layer may act to inhibit the ability of an incoming threat from locking onto select vessel infrastructures. Such an active system could protect critical navy assets both day and night by using seawater, directed through an array of nozzles, to produce an artificial obscurant shroud to attenuate thermally produced "hot-spots" and other regions of potential high contrast, to diminish a ship's signature. Additionally, the use of a smartly structured fog provides a method to create localized areas of obscuration without calling attention to the action and while minimizing the amount of liquid used to produce the result.

Background

The use of modern engineered obscurants is to defeat state-of-the-art reconnaissance systems such as satellites, drones or patrol aircraft, by disguising or spoofing a detection system. In addition to surveillance systems, obscurants are used to defeat anti-ship cruise missiles utilizing multi-band detectors. Modern sea protection systems are frequently standalone systems that launch spectrally tuned decoys, patterned arrays of decoys, and/or flares for seduction and/or distraction. However, the cost of including many of these systems translates into additional weight, reduction of deck space, and loss of valuable hold space. An alternative method would be to use seawater to generate localized fog patches, which are patterned (a spatial-temporal structuring) in such a way as to shroud selective ship infrastructure. This could be accomplished by the transient activation of an array of fog generating nozzles.

Method

1) Create a temporally and spatially controlled screening structure using water fog as an obscurant against imaging reconnaissance of identifiable features(shapes) within a size area of a few square meters.

2) Analyze the ability to identify obscured identifiable features(shapes), and to confuse imaging systems, using machine learning to increase our ability to do both, by leveraging our ability to structure an obscuring fog to maximize the difficulty to surveil. The obscuration structure is to be as imperceptible and efficient as possible while using readily available consumables such as sea water. The four main activities for the work are:

a. Use specifically spaced and timed fog mist nozzles to create a controlled volume of water fog across an area that is may be as large as several meters.

b. Record video images of the scene using the same camera systems that are used in reconnaissance scenarios in visible and infra-red wavelengths.

c. Design and use a neural network to analyze the scene images to best determine obscured shapes, and to evaluate fog plume interactions as feedback to the fog structure to provide best operation of the obscuration method (nozzle positions and timing).

This page intentionally left blank.

EQUIPMENT AND EXPERIMENTAL DESIGN

Large Environmentally Controlled Chamber

The experimental system was located with the Large Environmentally Controlled Chamber(LEC) at the Laboratory for Autonomous System Research at NRL. It is a large walk-in environmental chamber (11' X 10' X 10') designed for use to evaluate sensors and autonomous systems for temperature and humidity effects while simultaneously exposing them to test analytes at varying concentrations, and is ideal for this work. This chamber can be controlled from -30 to +185 degrees F and from 10% to 95% relative humidity. Our experiments were held at constant temperature of 21 degrees C, with varying humidities within the full range of the chamber.

Target Simulation System

A simulated target system is created by using thermal masks covering a controllably heated flat plate producing a near-blackbody source, see Fig. 1. The masks are made from opaque, 0.25 inch thick plastic sheets. Various shapes are cut out of the sheet and placed over the heated plate such that the mask defines a localized, heat induced radiation source that is the same shape as the cut out(Fig. 1, right side). The heated plate is a 4 ft. x 2 ft. aluminum slab with 1 inch thickness(Fig. 1-A). There is a 3/8 inch copper tube that snakes from one end to the other twice, which is used to flow heated water from a temperature controlled heat bath. The masked heat plate system is place vertically so that cameras can record the shapes from a horizontal distance, normal to the face of heat plate.

The heat bath is a ThermoCUBE® (Teledyne Princeton Instruments, 250 mL reservoir, 1 liter per minute flow, 5-50 ºC). This heat bath was able to control the heat of the plate to within 0.2 degrees within the range of 15 C to 50 C under an ambient atmosphere of 21 C. That is, a temperature difference range from ambient of about -6 C to 29 C.

The heated target shapes used were: squares, rectangles, polygons and hexagons. Several sizes for each shape were made, ranging from approximately 3 to 8 inches. There was enough room to place up to six different masks, horizontally across the heat plate.

When needed for initial calibrations, a 12’ x 12’ calibrated blackbody source (CI Systems, Inc., Controller Model SR-800N) was placed 6 inches above the target positions, and within the same field of view of the cameras to use as a temperature calibration for the infra-red cameras(Fig. 1-B). We also placed a 4 inch x 4 inch square piece of anodized aluminum directly below the heat plate for use as an ambient temperature target to use as a reference for each experiment run (Fig. 1-C).

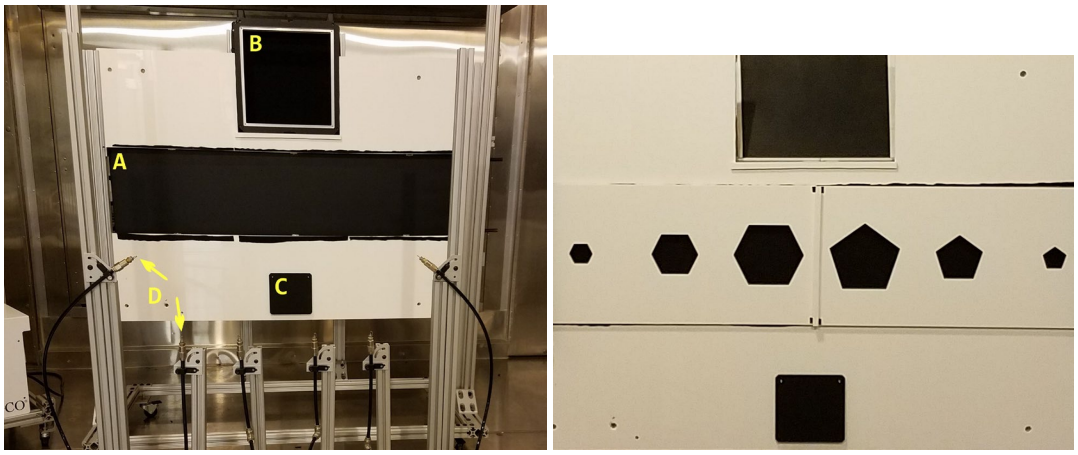

Figure 1: The heated target without(Left) and with shape masks(Right). A) The 1’ x 4’ heated plate. B) Calibrated blackbody source. C) 4” x 4” aluminum plate for ambient temperature measurements. D) Six fog generating nozzles are also shown in the left photograph. The photograph on the right shows, in closer detail, the masks over the heat plate allowing the infra-red emission from the plate to be seen through different sized hexagons and polygons.

Manuscript approved September 7, 2022.

Fog System

The fogging apparatus consists of the following components: A support structure that allows for the placement of fog producing nozzles. Six nozzles arranged on the structure, connected to a high pressure pump. Each nozzle is independently controlled by valves which are coordinated by computer using an in-house built control box.

The support structure(built separately from the structure that holds the heat plate) permits the placement of several nozzles surrounding a 2 m x 2 m area in order to fully cover the 1.5 m^2 area of the heat plate target. This structure was placed such that the nozzles were 30 inches in front of the heat plate. The nozzles can be directed in any direction within the area defined by the structure. Our typical use was to have four nozzles at the bottom pointing upwards, with two more mounted on the side with slightly higher than horizontal orientations to push fog across the area, from slightly below or above the center of the targets. (Nozzles, in one of our typical arrangements are shown as Fig. 1-D). Fig. 2 is a photograph from a aspect different angle, where the lower four nozzles are arranged along the line of site of the cameras, perpendicular to the heat plate. The cameras are not seen in the figure, but discussed in a following section.

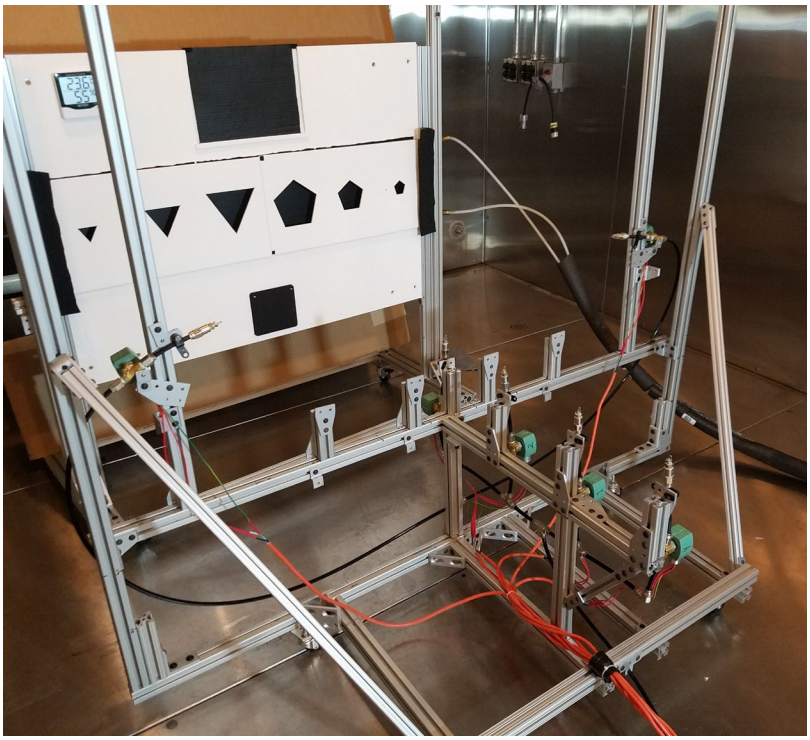

Figure 2: Another view of the nozzle structure and heat plate systems. The three nozzles closest to the heat plate are 30 inches from that plate, and the lower four nozzles are aligned along the site line of the cameras, which are to the right and not seen in the picture. Also in the photograph are the heated water lines connected to the right side of the heat plate(white plastic tubing, partially bundled in a dark insulation material), the individual valves for each nozzle(green boxes), an the individual electrical cables(orange) controlling each valve.

The nozzles used for fog creation are impingement nozzles with 50 µm orifices, and produce droplets that are initially 20 µm in diameter. The nozzles are actuated by individually triggered solenoid valves(ASCO™, Red Hat II™, Catalog No. 8262H200). These valves are rated for up to 1500 psi, and have a full open reaction time of approximately 0.3 seconds. The valves were placed as close as possible to the nozzles(about 3 inches) for best reaction times. The timing of the valves was orchestrated using Python scripts controlling a Raspberry Pi interfaced to solid state switches(Fig. 3). This allowed us to set up periodic patterning of the six nozzles, each with a maximum frequency of about 3 Hz (mechanical valve limited), and to work remotely from outside the chamber. Over the course of the project we used many different timing patterns, from constant output-all on, to complex

choreographed and periodic valve actuations. A water pump, (FOGCO®, Model #5150116) is used to maintain pressure to the nozzle system during each experimental run. By special order, we had this this pump made to handle salt as well as fresh water.

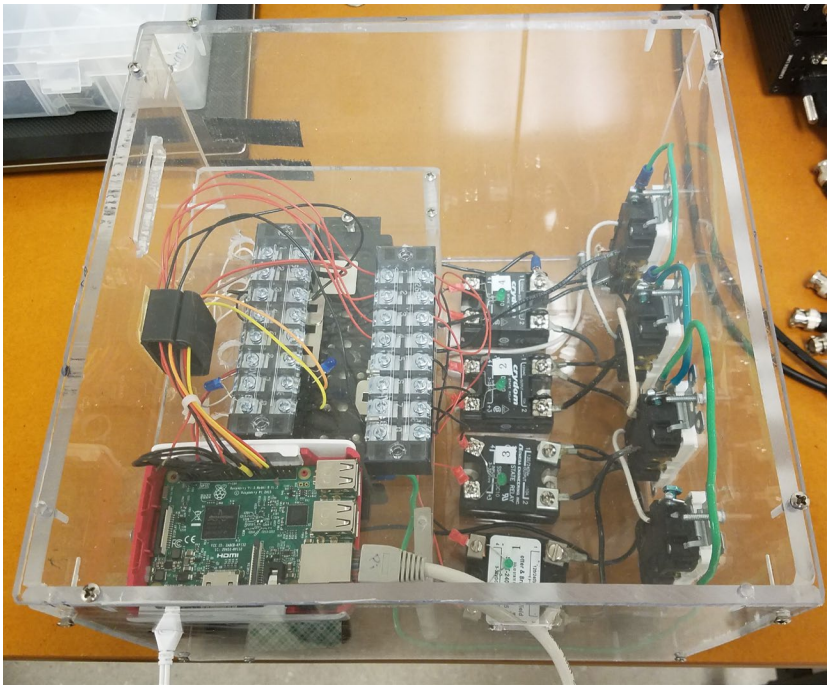

Figure 3: The Nozzle Control Box. A Raspberry Pi is programmed to control 6 valves using solid state switches.

Imaging System

The imaging system consists of 3 cameras, each with a different viewing bandwidth:

1) Visible	(400 - 800 nm)	- IO Industries (Victorem, 2KSDI-MINI)
2) A mid-infra-red	(3 - 5 µm)	- FLIR Systems, Inc. (A8200sc)
3) A long-infra-red	(8 - 14 µm)	- Sofradir-EC Inc. (Atom™ - 1024)

The cameras were mounted next to each other on a table located 130 inches from the heat plate within a humidity controlled enclosure. To record the videos during each experiment run, the cameras were monitored and recorded by two linked digital video recorders, from IO Industries (CORE 2 MAX). These have several terabytes of storage and provide simultaneous/synchronous recordings of all three cameras. Typically, the data was exported from these DVRs in two formats, compressed mp4, and individual video frames in the form of the lossless tif format. The software specific to the FLIR mid-wave camera, ("RIR" software) was used to record temperatures of the scene for each experiment.

Droplet density considerations

To complete the description for all aspects leading to a final light scattering analysis, we require the knowledge of the droplet densities and size distributions creating the fog. The number and size of droplets between the cameras and the target will determine how much obscuration will effect the images. To get an understanding of the size of droplets, an aerodynamic particle sizer (TSI, Model 3321) was placed near the heated plate and the nozzle apparatus soon after running the fog for several minutes, creating a near total-obscured image in visible wavelengths. (To avoid possible water damage to the instrument, we did not run it during the actual fog production.) Fig. 4 are photographs of the screen of the particle sizer when we first started recording droplet data, then again 35 seconds, and then at 55 seconds.

A dynamic change in size distribution can be seen with a peak of smaller droplets being measured in the latter two measurements, and with a large peak around 7 µm early on and persisting. The t = 0 picture is closer in time to what was being seen during the operation of the nozzles. The specification of the nozzles is 50 µm diameter droplets,

with an assumed normal distribution. The width of the distribution is unknown, but assumed to be determined by the pressure. Fig. 4 shows the distributions several minutes after the fog production, so only gives a general understanding of what the minimum size of the droplets were.

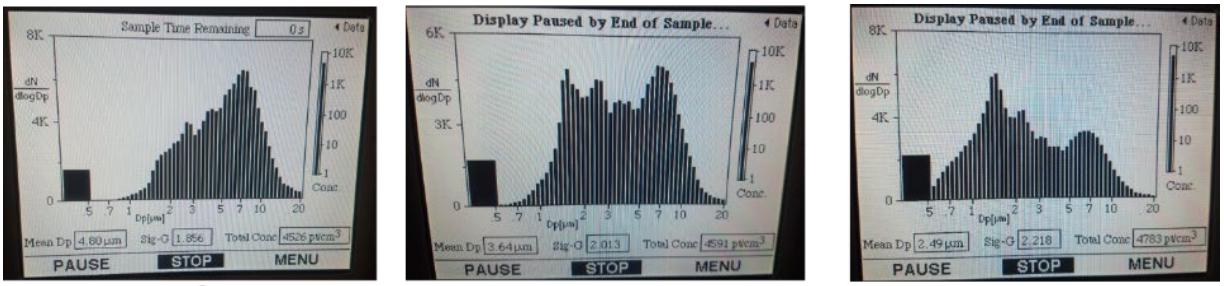

Fig 4. Droplet distributions in the LEC near the nozzles just preceding the droplet creation by about a minute. A peak of 7 μm diameter droplets persists while evaporation drives more droplets into the lower size bins over about a minute.

The conditions inside the LEC were stagnant air with an initially(pre-experiment) known relative humidity and temperature. During fog creation the humidity increased due to the evaporating droplets, and continued well as after the nozzles were turned off. The results of this demonstration are very specific, and do not closely mimic what is expected in real life situations, but it serves as a useful baseline for further experiments and modeling of water droplets within this chamber. Another source of valuable data is within the broad research of cloud formation. A typical cloud has a water density of 0.5 g/ m^3, in the form of randomly drifting droplets. Consider a rectangular volume one meter long and with 1 cm^2 cross sectional area as drawn within the fog zone between the masked heat plate and the cameras, Fig. 5. 10 μm diameter fog droplets are assumed and are randomly distributed within this volume.

Using the cloud density of 0.5 g/m^3 the number of droplets in the volume at any point in time would be 9.6 x 10^4, or roughly 10^5 droplets. To put this into perspective, if one were to place the droplets on a two dimensional plane, filling the cross sectional area of 1 cm^2, a total of 10^6 droplets would be needed (as shown lower right in Fig. 5). In this maximum fill case, 78.5% of the light passing through this volume would interact with the droplets, leaving the remaining 21.5% of the light as ballistic, passing through the open space between the stacked droplets. A single additional grid of 10^6 droplets could be placed behind the front grid, but off-set by a diameter, such that the space between the openings are then covered, allowing essentially no ballistic light. This would be a maximum case scenario to fully obscure the heat plate, ignoring the light scattering characteristics from the droplets as described above. Assuming a typical cloud density, we still have approximately a factor of 10 droplets too few to obscure the target in a unlikely scenario when they are lined up across the cross sectional viewing area. We could solve this by adding 10 meters of length to the scenario, thereby placing enough droplets with the volume to create a fully obscured view with perfectly placed droplets. The real life random placement of the droplets, however would always allow some ballistic light. Thus a volume defined by a 10 m length and 1 cm^2 cross sectional area could only be a minimum starting volume for which one would possibly observe “total” obscuration in this simplified model. Scattered light will be able to propagate through the drops to the cameras in cases of high forward scattering, depending on the wavelength of light and size of droplets. In case of much higher drop densities multiple scattering of light, from droplet to droplet, etc., will also play a role to diminish the ability of the light to pass through the volume, which is an additive process, and is described by an average extinction cross section of the droplet distribution in whole.

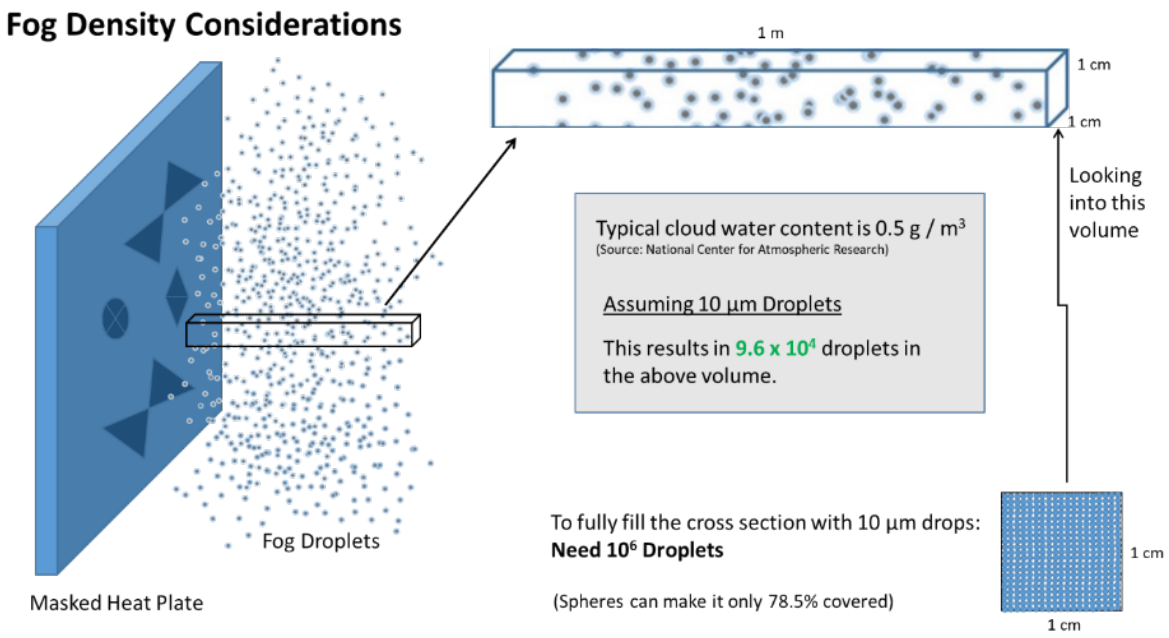

Figure 5: For total obscuration, a completely filled area as seen by the cameras, the density of droplets within a 1 meter length volume of 1 cm^2 cross sectional area requires nearly a factor of ten times the number of droplets of a typical cloud as defined by NCAR [Jaramillo, 2017 & Rinehart, 1969].

The instrument used in Fig. 4 provided us with an estimate of particle density across the entire range of sizes, up to 20 µm, which was about 4700 per cm^3, or a number density of 4.7 x 10^9 / m^3, which is 3 orders of magnitude larger than the simplistic scenario shown in Fig. 5, and 4 orders of magnitude larger than what is expected when comparing a typical atmospheric cloud. Pictures from the VIS camera and the LWIR camera of the masked, 50 C, heat plate just before the particle density measurements were taken are shown, in Fig. 6. The visible band camera is mostly obscured, while the wavelength bands 8 to 15 µm, from the LWIR camera, are still visible. (The cameras were looking though about 3.3 m of distance to the targets.) Also notable in these pictures is the ability to see through the same fog density using long wavelengths.

This was the only comparison we had looking at this aspect, and more data needs to be acquired, but at first glance, this provides us with a lower bound of a required number density for total obscuration in this system in the visible wavelengths. Methods to measure the density and size distributions of the produced fog are extensive, and techniques are being surveyed for consideration in further study that would be appropriate for our specific use in the large environmental chamber (LEC).

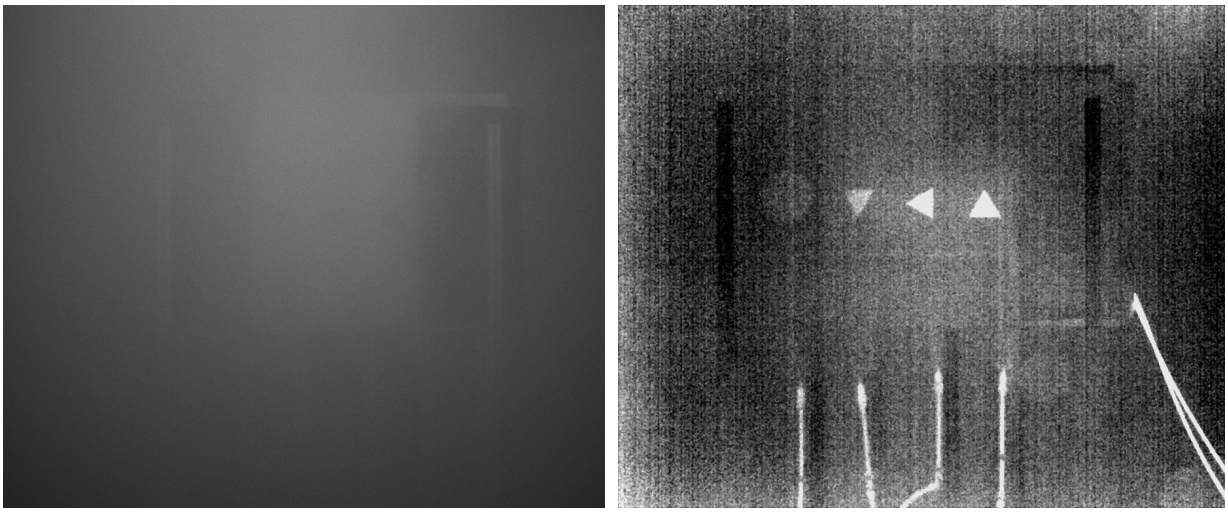

Fig. 6: Camera images in the Visible and LWIR bands in the LEC after filling the camber with fog leading up to the drop density measurements shown in Fig. 5. The particle sizing instrument indicated that there were 4 orders of magnitude more droplets than would be expected in a typical cloud containing 0.5 g/m^3 water density. The cameras are 3.3 m from the target plate.

Data Presentation

Data obtained during this project is primarily in the form of video images of the masked heat plates as various fog structures were formed in front of them. Using five different arrangements of the six nozzles, various temporally controlled valve actuation algorithms were implemented to create dynamic fog structures between the targets and the cameras. In all cases the nozzles were 30 inches from the heat plate and cameras were 100 inches beyond the nozzles. Fig. 7 shows the five layouts of the nozzles used to achieve different spatial densities. Nozzles are numbered as #1 - #4 below the heat plate and point upward, while #5 and #6 are pointing inward, but at an upward angle near horizontal at about 10 degrees, and are located just above the center height of the heat plate. The positions of #1 - #4 range from being lined up across the field of view with a spacing of 10 inches, to being lined up along the camera site line and 10 inches apart. The numbering of the nozzles is a permanent label on each specific nozzle in order to monitor the behavior over the experiment, and for reference in the program code controlling the timing. In configuration A), the lower nozzles were placed 23 inches below the center of the heat plate, in B) - E) they are placed 8 inched below the center of the heat plate in an attempt to generate higher droplet densities near target center. The labeling A) - E) in Fig. 7, are in chronological order with respect to the order of data acquisition, and trend towards increasing the density of the fog directly in front of the camera line of site.

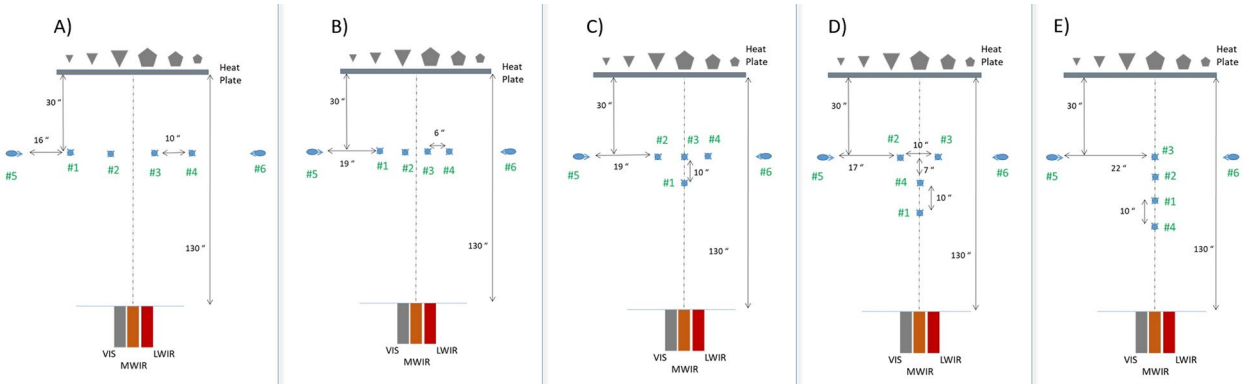

Figure. 7. The five different nozzle configurations used in the project. The labeling of A - E are in chronological order with respect to the order of data acquisition, and trend towards increasing the density of the fog directly in front of the camera line of site.

Approximately 600 data sets were recorded over the entirety of the project, (generating almost 3 TB of data), as we built up the system for the various nozzle configurations and finalized the camera settings for consistency in analysis. The last 60 data sets are the result of the most consistent procedures to control the cameras and recording parameters. Although the LEC is capable to adjust and maintain a desired relative humidity, the naturally high ambient humidities of the Summer months hampers the ability for the chamber to drop below 30% in a feasible time period. This lead to best data collection times, and best controllability in the Fall and Winter months.

Fig. 8 shows a composite photo of images from the three cameras with no fog in the chamber, and is typical of the video data sets used for general analysis. The nozzle configuration is the same as that labeled C) in Fig. 7. The lower half of the photograph is from the visible camera(VIS), where two nozzles can be seen (#5 and #6) on either side, and are at the approximately horizontal center of the target, with angle orientations of about 10 degrees from horizontal. The other four nozzles(#1 - #4) are located in the lower portion, pointing upward, and centered on the large hexagon to the right of (vertical)center. The upper section of the figure contains the two IR camera views, (left: LWIR, right: MWIR) which have been zoomed and cropped so that only the masked heat plate can be seen. Before cropping, both field of views of the IR camera match closely to that of the VIS camera. In the VIS camera portion in this image, the smaller dark square of the ambient temperature plate (labeled C in Fig. 1) can be seen, which is used to record the ambient temperature by the MWIR camera software before each data set is recorded.

The heat plate takes up the entire rectangular portion behind the shape masks causing the masking area over the plate to be to heated from behind. This can be seen in the two IR views, by the slightly bright rectangular areas surrounding the shapes (Refer to Fig. 1). For each data acquisition, the temperature of the masking material is measured using the MWIR camera, and recorded so that the temperature contrasts at the shape edges are known. For this particular data set, the ambient temperature was 23.0 C, that of the mask was 24.0 C with the temperature of the shape forms(heat plate) being 29.9 C. Imposed onto this image is the relative humidity of 15%, which is measured before every fogging acquisition run, and is from the LEC system sensor. The number in the lower left corner, 555 in this case, is the data run number for reference.

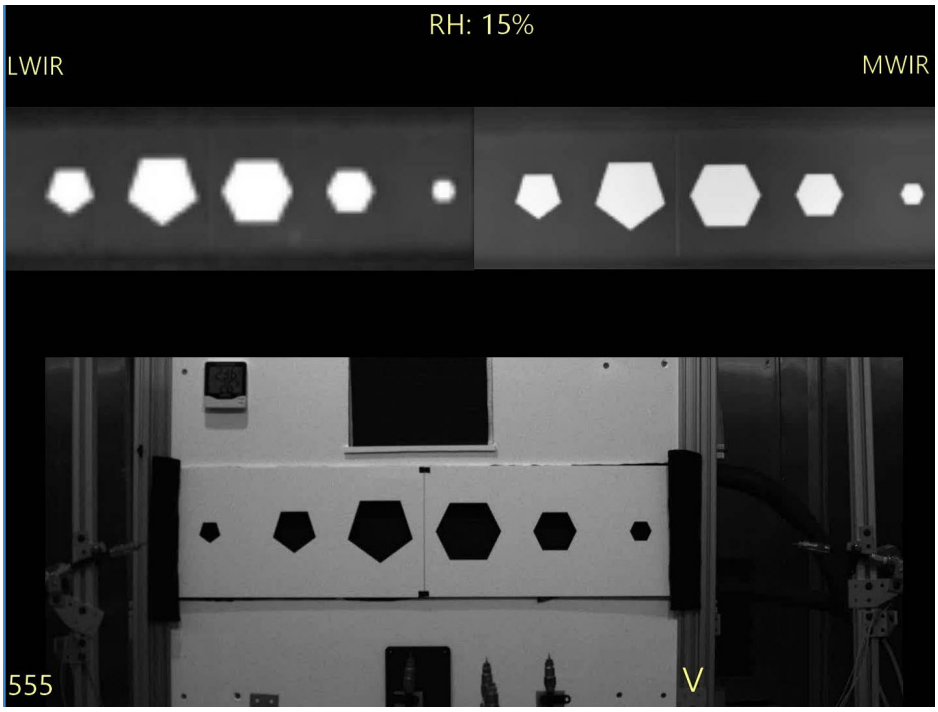

Figure 8. A frame composite from the three cameras just before the fogging system is turned on. (The nozzle locations are that shown in Fig. 21-C). The VIS camera is the bottom half and the two IR cameras are on top and cropped so that only the heat plate, with targets are shown.

Fig. 9 is the same composite image from the videos as Fig. 8, but taken a few moments after the as the fogging system was initiated. In this run, only the lower four nozzles were open, and with constant output. All three cameras were synchronized within a frame of record, which is within 1/30 of a second. In this frame the fog is seen to obscure more in the view of the MWIR camera than the LWIR, while the VIS camera shows a fog, but with much less obscuring.

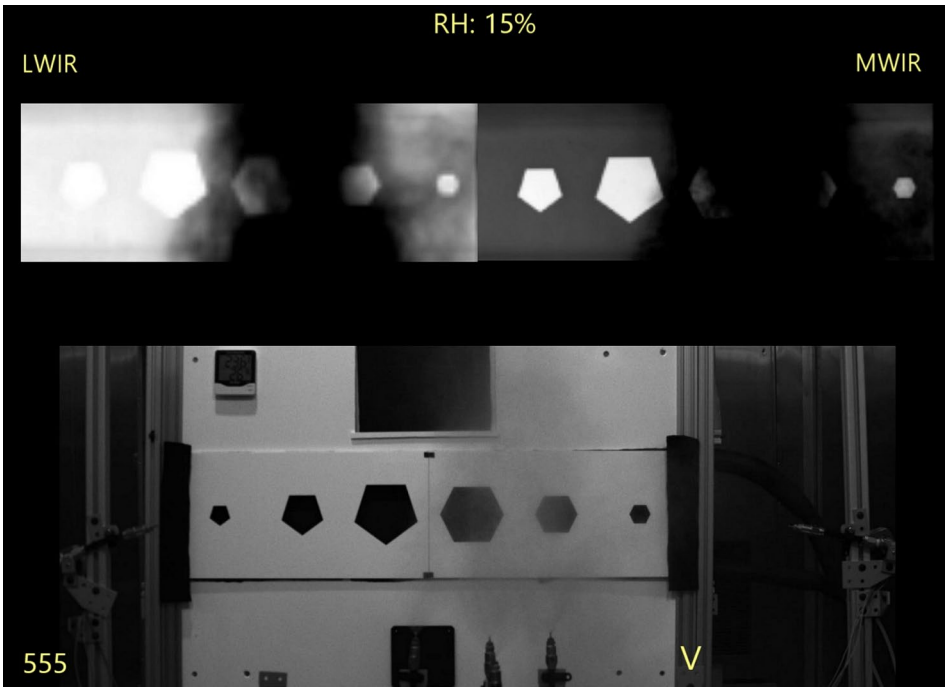

Figure 9. The same as Fig. 8, but several moments after the fogging system was started. In this case, only the lower four nozzles were actuated, and held open for constant output in time.

Two important points concerning the IR cameras should be noted for the data acquisitions:
1) LWIR camera was actively changing the contrast window throughout each video. When using the CORE 2 software to synchronously record the videos, we had no way of monitoring the LWIR camera settings in time as they changed with the dynamically changing scene.
2) The contrast window setting of the MWIR camera was constant throughout each video, and set before the fogging system was started, so that the contrast between the mask and the open portion defining the shape, was maximized for the no-fog scenario. We used the software of the CORE 2 to set the contrast window of the MWIR camera(not the RIR which is native to the MWIR camera). The DVR stores the data in raw form, and this setting is applied post-process before saving the final version of the image data, such as that shown in Fig. 9. This allows us to go back anytime to re-process the MWIR output using a different contrasting window.

The dynamics of a changing scene is a important feature of this project, and the static images only exemplify the droplet density movements and obscuration transformations created by the flowing fog to a small extent. The videos of the data acquisitions are most useful for analysis, and are available for the interested reader. In this report, we attempt only to showcase a few results using static images from the frames of recorded videos. Figs. 10 & 11 are examples of the different nozzle configurations shown in Fig. 7. Fig. 10 left and right correspond to layouts in A) and B) in Fig. 7, and Fig. 11 left and right correspond to D) and E) in Fig. 7, respectively. Like Fig. 9, both Figs. 10 and 11, also have data reference numbers imposed on the lower left of each image. Although the static frame images do not convey the overall results of the video, as a matter of example record, the experimental conditions, including the orchestration of the nozzle timing for each data set, is listed in Table 1 for the Figs. 10 and 11, where each image is used listed according to reference number.

Reference	Heat Plate Temperature [C]	Mask Temperature [C]	Ambient Temperature [C]	Relative Humidity [%]	Nozzle Timing Pattern
485	48.0	27.2	27.2	60	Constant All
520	27.0	23.4	22.3	70	Random All 0.3 sec switching
558	29.8	23.8	22.9	50	Constant All
598	29.9	23.9	22.9	13	Sequential 1, 2, 3, 4 Alternate 5, 6 0.5 sec switching

Table 1. Experimental conditions for videos in data sets shown in Figs. 24 and 25.

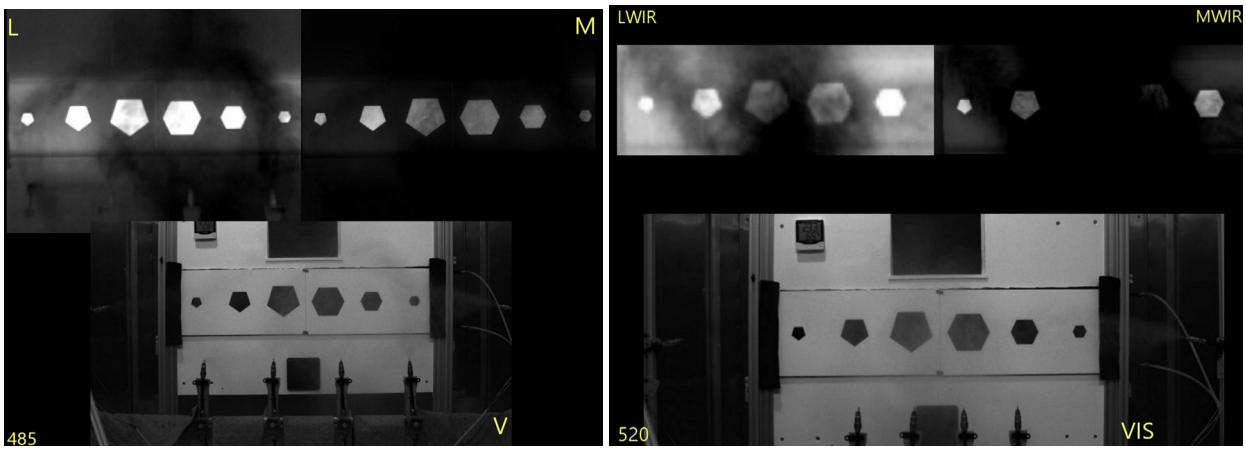

Figure 10. Nozzle configurations of left and right images correspond to layouts A) and B) in Fig. 7, respectively.

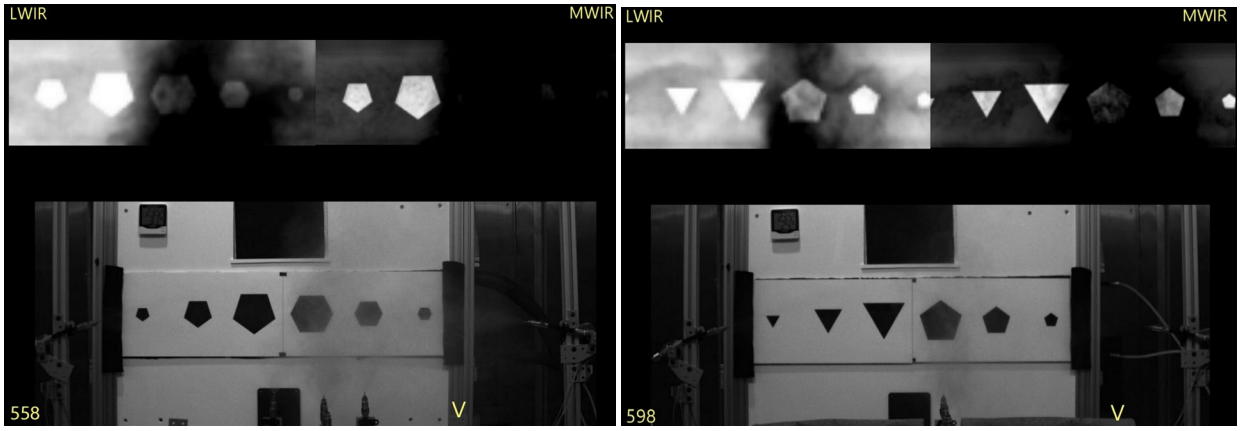

Figure 11. Nozzle configurations of left and right images correspond to layouts D) and E) in Fig. 7, respectively.

Fog Results General Observations / Conclusions

There are several general observations when analyzing the video data.

1) Camera settings.

The LWIR band camera generally performs better in all videos due to the real time, dynamic windowing of the contrast during a fogging event. The camera did not however report/record the windowing values during the experiments. The MWIR however, typically showed more obscuration of the targets, but could have similar results to the LWIR, because the contrast window of the MWIR camera was static during the experiments. However, this made it so that the contrast settings of the MWIR camera were always known.

The data recorded by the CORE 2 software allows for the MWIR settings to be changed before exporting to the final images and could be re-exported with different, and even ideal contrast settings, allowing the MWIR camera to "see" better than when originally set, and possibly even better than the LWIR camera. Except for a few exploratory data sets, this activity was not yet performed during this work, but given additional time, the original raw data stored on the CORE DVRs could be post-processed in this way. Further analysis to better quantify camera settings needs to be performed on the data obtained during this project. Cameras have the ability to modify contrast windowing in real time, and thus makes the need to quantify the results in terms of optimum settings over the course of the entire viewing period, frame by frame, most important. Video data that incorporates a metadata channel that also records this type of information would be best for future work in this area.

2) Effects of the ambient relative humidity.

There were consistent observations how the relative humidity effected the results. The data sets reliably showed higher obscuration in both cameras in lower ambient relative humidities compared to that of high humidities. Fig. 12 is a static example of comparable fogging runs, each with very different humidities. The frames being compared in Fig. 12 were chosen due to the closeness of the fog densities in the images when looking at the VIS portion of each. In both cases all fog nozzles were running at constant output through out the recordings and in configuration shown in Fig. 7 - D. The left image(556) is from a run that had initial LEC humidity of 17%, and the one on the right (561) was at 80%. The regions of interest of the two camera views have been circled green and orange for the LWIR and MWIR cameras, respectively. In both cases, the view in the 80% initial RH shows more visibility of shapes through the fog than the 17% RH. It is to be expected that in higher RH conditions, the droplets will evaporate less, and thus create a size distribution that contains larger droplets than would be present in lower RH atmospheres. Larger droplets generally scatter more in the forward direction, resulting in more light passing onto the cameras after interacting with the droplets, than from smaller droplets, which tend to scatter more light into the non-forward directions. Additionally, the fog droplets in a lower RH atmosphere will generally be cooler providing additional black body radiation at longer wavelengths, potentially interfering more with the target image with greater contrast, than that from the warmer droplets in the higher RH atmosphere(less contrast).

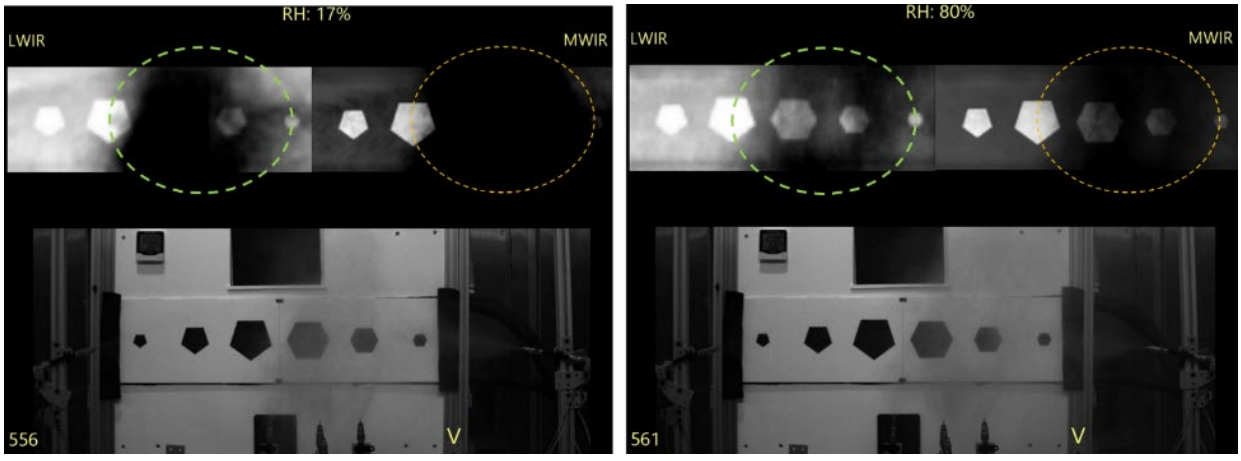

Figure 12: Example of comparable fogging runs, each with very different humidities. The image 556 is from a run that had initial LEC humidity of 17%, and the one on the right, 561, was initially at 80%. The regions of interest of

the two camera views have been circled green and orange for the LWIR and MWIR cameras, respectively. In both cases, the view in the 80% initial RH shows more visibility of shapes through the fog than the 17% RH.

3) Spatial and temporal effects of obscuration.
We found that spatial differences in nozzle placement produced the expected results for the creation of higher density fog plumbs. Although data from the more spaced nozzle configurations, such a that shown in Fig. 7 A, did have dynamic obscuration events during the videos in the IR cameras, the visible wavelengths were not effected until we started using the narrower spaced designs of Fig. 7 D and E. In this work, we never did achieve full obscuration in the VIS using temporally pulsed nozzles at any spacing, and even with the narrowest of spaced nozzles only partial. See Fig. 12, as an example.

We used nearly 70 different nozzle control algorithms that varied which nozzles were actuated and the timing of the actuations during this work. These included random actuations and structured sequences using different pulse times. Pulse times used were 0.5, 0.3, 0.1 and 0.05 seconds. These algorithms can be found along with the video data archive. We were able to achieve non-permanent obscurations using many of these sequences, but found no specific pattern that would achieve a total obscuration over the length of the data set that compared well with that from a constant output scenario. We did observe that moderate lengthed pulses of 0.1 to 0.3 seconds were as good as 0.5 seconds and some continuous output. These sets present a starting point for more quantification of structured fog in future work, it also provides a basis for the possibility to be more efficient when it comes to this type of fog obscuration technique. The shorter timed pulses of 0.1 and 0.5 seconds were on the edge or below the reaction time of the valves, and tended to produce less dense fog, and poor obscuration.

4) Droplet sizes and number densities.
Using the structured fog approach, we observed only minimal obscuration in the visible camera. It was only by filling the chamber with fog and creating a situation that obscured the image for the visible camera did we achieve this(Fig. 6). By performing a droplet number density (and size distribution) measurement during this time we were able to estimate that we had several orders of magnitude more droplets than what was minimally required to obscure the target in the visible wavelength band. Although this is informative and helped allow us to understand the end points of the problem, we can only infer the densities from our structured fog system based on these loose estimates. A system to directly measure droplet densities will be needed in future work in this area.

Digital Analysis of the Videos

1) To assist in the development of the analysis algorithm a synthetic dataset was produced. This dataset consists of five different shapes (triangle, square, rectangle, pentagon, and hexagon) with scattering affects. The synthetic measurement is the result of three operations (caused by the scattering fog):

1. Exponential falloff in intensity
2. Blurring of image
3. Additive background light

Instantiations of fog patterns were computed using a turbulent flow map generator in MATLAB. This map was rescaled between [0, 1] and represented the amount of fog occurring at that pixel. This value would affect operations 1 and 3. After all operations, Poisson noise was added. Different fog instantiations resulted in different samples. This simulated dataset was meant to be a quick method to generate “foggy” images to test metrics with. It is not meant to be physically realistic: it is limited in the sense that it does not model light rays and the scattering media is only 2 dimensional.

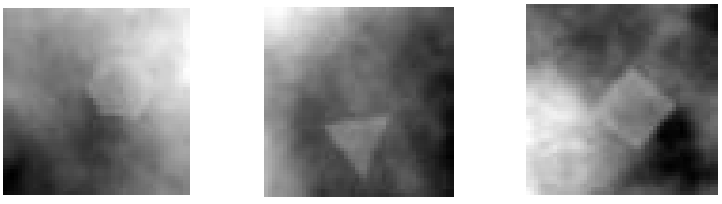

Figure 13: Examples of simulated obscured shapes using a turbulent overlay.

2) Preparation of Experiment Data

Each frame of the experimentally captured videos was appropriately cropped around the region of interest(ROI) where a shape was contained. These resulting images were then passed through an augmentation pipeline to introduce rotations, translations, and intensity variations.

3) Definition of Obscuration Metrics

Before analyzing any of the captured data, it must be established how *obscured* the target is when utilizing different fog patterns. Computing the cross-correlation between the known ground truth and the obfuscated target can provide a naïve estimate of how well concealed the target is due to the fog. However, we should expect our adversaries to be using state-of-the-art techniques to decipher what is being concealed. With that in mind, we plan to demonstrate obscuration using classification accuracy from a neural network. Neural networks have shown state-of-the-art classification performance in several tasks and will show the best detection accuracy for a standard passive imaging system (not time-of-flight) imaging through scattering media. We define classification accuracy here as the number of correctly classified shapes divided by the total number of images within the validation dataset.

3) Description of Networks Used

We wanted to investigate off the shelf networks that have achieved state-of-the-art performance in shape/image classification. We examined a number of networks supported by the Python computing language module torchvision. We initially chose a basic convolutional neural network (CNN) to build an foundational level of understanding of the fog images, then based on the performance of ResNet50 and DenseNet in [Neary, 2020 & Kaiming, 2015], we chose those two more methods to investigate more deeply.

When applying the CNN, we increased the number of convolutional layers and pools to test the system against the gathered experimental images. Experimental images were the individual video frames of the fogging experiment, which varied in time, providing views ranging from completely obscured to nearly no obscuration at all. Those frames which there was minimal obscuration were grouped and used as training sets for the highly obscured testing images. Table 1 is a result as the number of layers and pools were increased. A maximum accuracy was reached for 6 layers and 4 pools.

Table 2: Test accuracy for increasing the number of layers and pools in the CCN tests.

Network	Test Accuracy
2 Conv, 1 Pool	.366
3 Conv, 2 Pool	.788
4 Conv, 3 Pool	.843
5 Conv, 4 Pool	.880
6 Conv, 4 Pool	.902
7 Conv, 4 Pool	.900

A more informative view, and a test of the algorithm of the CCN is to display the results within a confusion matrix, which directly compares the test images with the true solution. Fig. 14 is an example of results shown in a confusion matrix of images tested with and without obscuring fog. The left table in Fig. 14 shows the results using images of one possible single shape: triangle, square, rectangle, pentagon, or hexagon. This set, as expected, shows a highly accurate model to predict what shape was in the frame, while on the right side of Fig. 14, images with high amounts of obscuring fog covered the shapes with promising, but less accurate results.

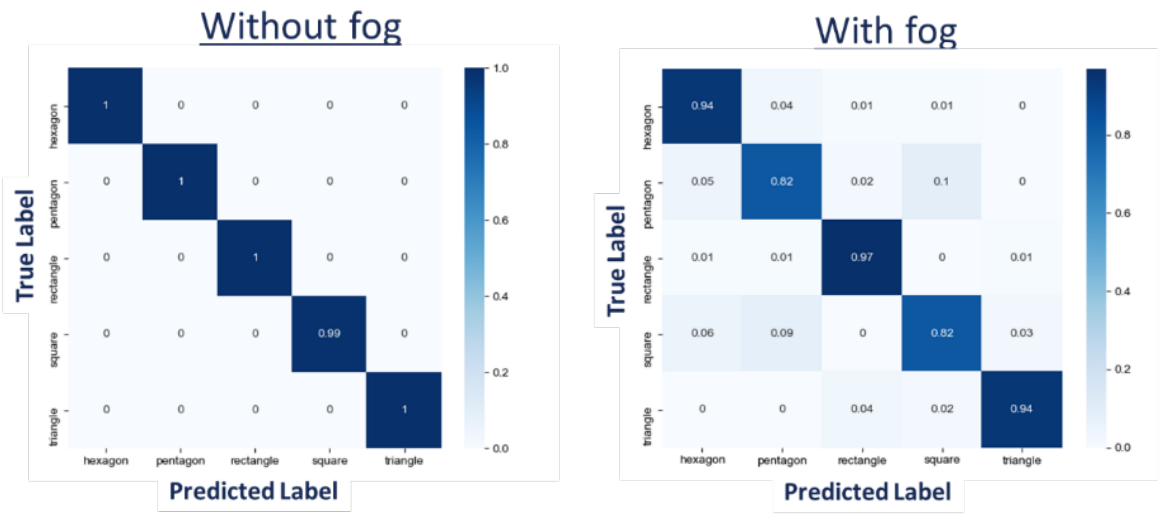

Figure 14: Confusion matrices for CNN tests. The left table illustrates the ability to perfectly predict the unobscured shapes, and the table on the right shows an example of results from a set of images obscured with fog. In any of the images, one possible shape could be in the scene: triangle, square, rectangle, pentagon, or hexagon.

Fig. 15 shows an example set that was particularly difficult to determine with accuracy. The shape labels in the figure are what the CNN misidentified.

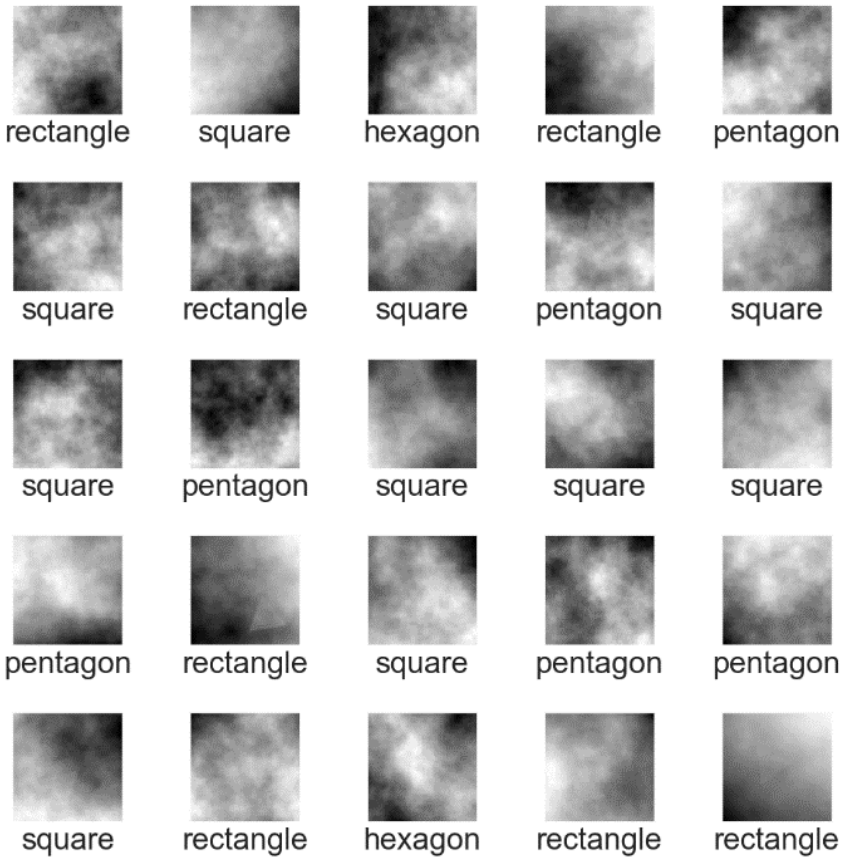

Figure 15: A set of difficult to identify scenes, where an incorrect label was assigned by the CNN.

After working with the basic CNN, we expanded our ability using ResNet50 and DenseNet.
ResNet50 is a convolutional network 50 layers deep that contains residual layers that have a reference to layer inputs. This alleviates some of the issues with training very deep neural networks. DenseNet is a similar formulation to ResNet50, however it concatenates the inputs of other layers rather than adding the inputs. It tends to also use less parameters. Pretrained versions of these networks were initialized and further trained using simulated or experimentally captured tested datasets. Training and testing occurred on an NVidia RTX 2080 8GB graphics card using PyTorch.

4) Characterization of Different Networks
Table 3 shows a comparison of performance (in accuracy), number of parameters and runtime of a number of state of the art neural networks at the time of writing for image classification. These methods are implemented in torchvision models. ResNet shows the best performance while maintaining a reasonable runtime using initial layers similar to that shown in Figure A-1 in the Appendix.

Table 3: Testing networks on all datasets with FLIR (MWIR) camera.

Network	ShuffleNet	SqueezeNet	MobileNet	DenseNet	ResNeXt	ResNet	AlexNet	WideResNet
Performance	.606		.694	.686	.721	.742		.706
Num Params	347972		2231588	6960036	22992228	23520356		66846564
Runtime (s)	92.0		76.3	188.3	97.6	91.8		138.6

Table 4 compares different performance metrics between ResNet50 and DenseNet on experimentally collected data from the midwave camera. The experiment configuration for these results is such that all 6 nozzles were continuously on. Results are shown with and without cross validation. Cross validation is a way to resample limited data into many different iterations of training and testing data. Based on the resampling factor K (in this case 5), the data is broken up into K blocks and K-1 are used for training while 1 is used for validation. This is repeated K times so that each group has the chance to be the test data. Accuracy is then averaged across all iterations.

Table 4: Table comparing different performance metrics between ResNet50 and DenseNet.

Previous results: no cross validation

Testing two networks on FLIR 436 database

ResNet-50	DenseNet121
0.741	0.710

Testing ResNet-50 on 3 different databases

FLIR 436	VIS 436	LWIR 436
0.741	0.976	0.999

Testing ResNet-50 on FLIR 436 with different learning rates

2e-5	1e-5	1e-4
0.741	0.689	0.761

Testing best network on FLIR 436 with different number of epochs

6	10	30
0.741	0.727	0.730

Testing best network on FLIR 436 with different image sizes

100x100	50x50	200x200
0.741	0.723	0.707

With cross validation (K=5)

Testing two networks on FLIR 436 database

ResNet-50	DenseNet121
0.725	0.702

Testing ResNet-50 on 3 different databases

FLIR 436	VIS 436	LWIR 436
0.725	0.996	0.999

Testing ResNet-50 on FLIR 436 with different learning rates

2e-5	1e-5	1e-4
0.725	0.720	0.724

Testing best network on FLIR 436 with different number of epochs

6	10	30
0.725	0.723	0.744

Testing best network on FLIR 436 with different image sizes

100x100	50x50	200x200
0.725	0.720	0.721

Summary and Discussion

During this project, we demonstrated the ability to simultaneously record three wavelength bands ranging from 400 nm to 14 μm from specifically shaped blackbody radiation sources through a curtain of structured fog. The structured fog was created by using up to eight temporally coordinated water mist nozzles in several spatial arrangements. The data acquired was in the form of a video record where each frame of a video was used as a data point to compare the three cameras at concurrent points in time. We then demonstrated machine learning(ML) based shape analysis using the images from each video frame, where the images were used for either training or testing the ML algorithm.

The temporally and spatially controlling fog plumes in a small area were evaluated using the video records as well as visually. The effectiveness of the operation was found to be inconclusive. It was apparent that even though certain time periodic structures can increase the fog density in a smaller or larger portion of the area, the scene remains dynamic and can quickly change to an openly viewable scene with little obscuring fog in the region of interest, revealing the hidden shape. The natural turbulence of the system is the main hurdle for the goal in this work, as controlling that aspect is an exceedingly challenging undertaking. Except for during short time spans, when higher then natural droplet densities were produced, there were no cases when we observed our fog structuring to be superior to that created from a constant, dense fog situation with all nozzles in continuous operation. In the continuous operation, the result of the fogging system was also hindered by the unavoidable turbulence.

From this work, it has been made clear that by providing a method to more actively force droplets into a static configuration, rather than attempting to control the turbulent behavior, one could achieve the type of limited area and subtle obscuration desired using water fogs. Extending this current research to methods that utilize acoustic control of droplets, for instance, may provide the desired result. Although we did not come to a positive conclusion on the effectiveness of the structuring of fog, the techniques developed in this project provide a foundation for obscuration testing methods moving forward using data gathering and state-of-the-art machine learning techniques, similar to what an expected adversary would use from a surveilling platform.

APPENDIX - Neural Network Background

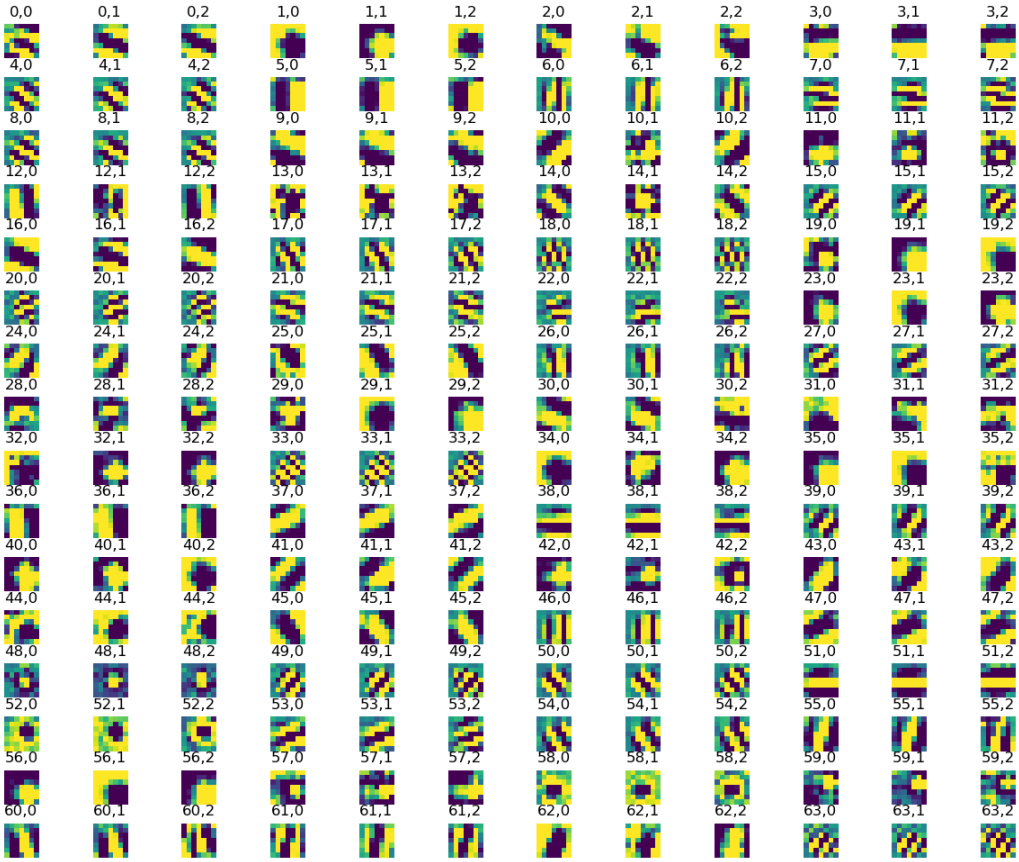

Figure A-1: One of the initial layers of ResNet50. Visualizing the filter weights demonstrating extracting certain edge features from the input images.

REFERENCES

Jaramillo, A., “Notes and Correspondence On the relative density of clouds ,” Q. J. R. Meteorol. Soc. **143**: 2650-2653, 2017.

Rinehart, G. S., “Fog Drop Size Distributions - Measurement Methods and Evaluation,” Atmospheric Sciences Laboratory, White Sands Missile Range, NM, Report DA Task 1T061102B53A-2D, ECOM-5247, April, 1969.

Neary, Patrick L., et al. "CNN Classification Architecture Study for Turbulent Free-Space and Attenuated Underwater Optical OAM Communications." Applied Sciences 10.24: 8782, 2020.

He, Kaiming, et al. "Deep residual learning for image recognition,” CoRR abs/1512.03385: 646-661, 2015.